

# Spectral analysis of geomagnetically induced current and local magnetic field during the 17 March 2013 geomagnetic storm

**Wen-Hao Xu**

Shandong University School of Mechanical Electrical and Information Engineering

**Zan-Yang Xing** (✉ [xingzanyang@sdu.edu.cn](mailto:xingzanyang@sdu.edu.cn))

Institute of Space Sciences, Shandong University <https://orcid.org/0000-0001-5965-1017>

**Nanan Balan**

Institute of Space Sciences, Shandong University

**Li-Kai Liang**

Shandong University School of Mechanical Electrical and Information Engineering

**Yan-Ling Wang**

Shandong University School of Mechanical Electrical and Information Engineering

**Qing-He Zhang**

Institute of Space Sciences, Shandong University

**Zi-Dan Sun**

Shandong University School of Mechanical Electrical and Information Engineering

**Wen-Bin Li**

Shandong University School of Mechanical Electrical and Information Engineering

---

## Full paper

**Keywords:** Geomagnetically induced current (GIC),  $dBx/dt$ , geomagnetic storm, Cross Wavelet Transform (XWT), Wavelet Coherence (WTC)

**Posted Date:** March 25th, 2021

**DOI:** <https://doi.org/10.21203/rs.3.rs-342899/v1>

**License:** © ⓘ This work is licensed under a Creative Commons Attribution 4.0 International License.

[Read Full License](#)

---

**Version of Record:** A version of this preprint was published at Advances in Space Research on February 1st, 2022. See the published version at <https://doi.org/10.1016/j.asr.2022.02.025>.

---

# Spectral analysis of geomagnetically induced current and local magnetic field during the 17 March 2013 geomagnetic storm

Wen-Hao Xu<sup>1</sup>, Zan-Yang Xing<sup>2,\*</sup>, Nanan Balan<sup>2</sup>, Li-Kai Liang<sup>1,\*</sup>, Yan-Ling Wang<sup>1</sup>,  
Qing-He Zhang<sup>2</sup>, Zi-Dan Sun<sup>1</sup> and Wen-Bin Li<sup>1</sup>

<sup>1</sup>*School of Mechanical, Electrical and Information Engineering, Shandong University, Weihai, Weihai, Shandong, 264209, China*

<sup>2</sup>*Shandong Provincial Key Laboratory of Optical Astronomy and Solar-Terrestrial Environment, Institute of Space Sciences, Shandong University, Weihai, Shandong, 264209, China*

Corresponding author: Zan-Yang Xing([xingzanyang@sdu.edu.cn](mailto:xingzanyang@sdu.edu.cn)) & Li-Kai Liang ([lianglikai@sdu.edu.cn](mailto:lianglikai@sdu.edu.cn))

## Key Points:

- The CWT and DWT spectrographs of GIC and dBx/dt during the 17 March 2013 storm are very similar.
- The XWT and WTC spectra of GIC and dBx/dt reveal their correlation and phase relationship for the first time.
- The third-order low frequency coefficient best reflects the disturbances in GIC and dBx/dt.

**Abstract:** Geomagnetically induced current (GIC) is known to be closely related to the rate of change of local horizontal magnetic field (dBx/dt); and their spectra can give better insight into the relationship. We study the spectral characteristics of GIC measured in Finland and dBx/dt measured 30 km away during the 17 March 2013 intense geomagnetic storm (SymHMin = -132 nT). Two bursts of large GIC (up to 32A) and dBx/dt occurred at ~16 UT and 18 UT during the storm main phase, though

---

28 their values were generally small. For the first time, the Cross Wavelet Transform  
29 (XWT) and Wavelet Coherence (WTC) techniques are used to investigate the  
30 correlation and phase relationship of GIC and dBx/dt in time-frequency domain. Their  
31 WTC correlation is strong (over 0.9) over the entire storm period, indicating dBx/dt is  
32 the main factor causing GIC and dBx/dt leading GIC. Their XWT spectra show two  
33 enclosed periods (8-42 min and 2-42 min) in the high energy region corresponding to  
34 the two bursts of activity in GIC and dBx/dt. Moreover, we use continuous wavelet  
35 transform (CWT) and discrete wavelet transform (DWT) to analyze the spectral  
36 characteristics of GIC and dBx/dt. It is found that the CWT and DWT spectra of the  
37 two are very similar, especially in the low frequency characteristics, without  
38 continuous periodicity. Wavelet coefficients become large when GIC and dBx/dt are  
39 large; and the third-order coefficient, which corresponds to low-frequency part, best  
40 reflects the disturbance of GIC and dBx/dt.

## 41 **1. Introduction**

42 GIC (geomagnetically induced current) is the final link in the space weather chain  
43 originating from the sun. The high speed high density solar wind and frozen-in  
44 magnetic field (called solar storm) ejected from the sun propagates through the  
45 interplanetary space. The solar storm interacts with earth's magnetic field and  
46 generates large electric current in the magnetosphere leading to geomagnetic storms;  
47 and the current terminates mainly in the high latitude ionosphere. The magnetic field  
48 produced by the large ionospheric current propagates down to the earth and induces  
49 secondary current (called GIC) in the earth by Faraday's law; and GIC flows through  
50 the earthed utility systems such as electric power grids, tele-communication networks,  
51 oil and gas metal pipe lines, railway signal systems, etc. ([Gideon et al., 1970](#);  
52 [Campbell, 1978](#); [Pulkkinen et al., 2001](#); [Liu et al., 2009](#)). During extreme space  
53 weather events, GIC can exceed the tolerance limit of the systems and cause system  
54 damages as happened during a number of such events ([Carrington, 1859](#); [Albertson  
55 and Thorson, 1974](#); [Bolduc, 2002](#); [Pulkkinen et al., 2006](#)). Even medium level GIC  
56 flowing for a long period of time can cause cumulative impacts on utility systems

---

67 through reactive power loss in transformers, corrosion in pipe lines, etc., which can  
68 pose significant risk especially when there are defects in the systems (Viljanen et al.,  
59 2001; Eroshenko et al., 2010; Khanal et al., 2019).

60

61 In addition to the global cause originating from the sun, GIC depends on local  
62 factors such as ionospheric and earth electrical conductivities (Pirjola, 2000). At high  
63 latitudes, auroral zones are associated with the flow of auroral jets in the ionosphere.  
64 During storms, this current system can be strongly enhanced by magnetospheric  
65 substorms, resulting in large GICs on the ground (Ngwira and Pulkkinen, 2019). The  
66 rate of change of local horizontal magnetic field ( $dB_x/dt$  or  $dB_h/dt$ ) is found to be a  
67 good indicator of GIC (Viljanen et al., 2001), with  $B_x$  being the northward component  
68 of the resultant horizontal field  $B_h$ . A number of scientists have shown good  
69 association between GIC and  $dB_x/dt$  (and  $dB_h/dt$ ) (Trichtchenko and Boteler, 2004;  
70 Tóth et al. 2014; Dimmock et al., 2019; Heyns et al., 2020; Juusola et al., 2020). In  
71 addition, spectral analysis techniques have been used to obtain better insight into the  
72 relationship (Mendes, et al., 2005; Xu, 2011; Falayi et al., 2017; Adhikari et al., 2017).  
73 Since GIC is a non-stationary periodic signal that is continuously transformed in time,  
74 Continuous Wavelet Transform (CWT) has been used for spectrum analysis, and the  
75 signal has been observed from the time domain and frequency domain at the same  
76 time (Xu, 2011). Using the advantages of CWT for multi-scale analysis of the  
77 characteristics of each frequency band of the signal, the data can be analyzed on time  
78 and space scales, and localized characteristics of the signal can be observed. Xu (2011)  
79 separated the geomagnetic effect caused by the magnetosphere and ionosphere by  
80 observing the changing frequency of GIC.

81

82 Falayi et al. (2017) used CWT to perform spectrum analysis on GIC and found  
83 that GIC corresponds well to the high-energy wavelet coefficients of  $dB_x/dt$ . Khanal  
84 et al. (2019) used CWT to analyze the GIC data caused by high-intense long-term  
85 continuous auroral activity, and found that GIC has short-term energy bursts and  
86 continuous energy distributions with different periods. With an anticipation to

---

87 establish a forecasting tool for surface geomagnetic disturbances, [Adhikari et al.](#)  
88 [\(2017\)](#) used CWT and DWT to analyze the GIC data during four strong and weak  
89 magnetic storms, and found that the GIC has a stronger power spectrum in response to  
90 higher intense magnetic storms. [Ariannik, et al. \(2020\)](#) proposed a method of using  
91 CWT to reduce noise and calculate the event derivative of the geomagnetic X  
92 component to predict the size of GIC. However, earlier studies have not used CWT  
93 and DWT together to study both GIC and geomagnetic data. Moreover, the  
94 cross-wavelet technique can analyze the correlation between the high-energy and  
95 low-energy regions of two time series in the time-frequency domain from multiple  
96 time scales, reflecting the phase structure of the two; and it has been widely used in  
97 geography and physics ([Li et al., 2020](#)). However Earlier studies not analyzed the  
98 correlation between GIC and geomagnetic data using crossed wavelets. In this paper,  
99 the cross wavelet technique is applied to this field for the first time

100  
101 In this paper, we first use CWT to analyze the spectrum of GIC and dBx/dt  
102 measured in Finland during the intense geomagnetic storm (SymHMin = -132 nT) of  
103 17 March 2013. Then DWT is used to analyze the wavelet coefficient characteristics  
104 of GIC and dBx/dt and obtain the correlation between GIC and dBx/dt. It is found that  
105 there is a great degree of similarity between the two. Therefore, finally, the cross  
106 wavelet technique is used to analyze the correlation and phase characteristics between  
107 GIC and dBx/dt in time and frequency domain.

## 108 **2. Data and analysis techniques**

109 We use the 10-second resolution GIC data measured ([Pulkkinen et al., 2001](#)) in  
110 the Finnish natural gas pipeline at Mancelai (MAN, 60.6°N, 25.2°E) during the  
111 geomagnetic storm on 17 March 2013; data are available at  
112 [http://space.fmi.fi/gic/man\\_ascii/](http://space.fmi.fi/gic/man_ascii/). The corresponding northward magnetic field Bx  
113 measured by the reference magnetometer at Nurmijarvi (NUR, 60.5°N, 24.7°E) 30 km  
114 away from MAN is available at <https://space.fmi.fi/image/www/index.php>; it is used  
115 to calculate the 10-second resolution dBx/dt. The pipeline in the area where the NUR

116 station is located is mainly east-west. Accordingly, it is more reasonable to select the  
 117 geomagnetic northward component Bx to explore the relationship with GIC (Viljanen,  
 118 2006). The 30 km spatial separation between the MAN and NUR stations and other  
 119 factors can cause a small error in GIC. As an overall estimate, the error is ~0.1A and  
 120 inaccuracy due to various reasons is ~10-15% (Pulkinen et al., 2001).

121

## 122 2.1. Continuous wavelet transform (CWT)

123 CWT continuously describes the changes of the signal in a detailed form on  
 124 different time scales, and is suitable for studying GIC time series and finding time  
 125 periods where high power is concentrated during events. For a given time series  $f(t)$ ,  
 126 the wavelet transform is expressed as (Torrence and Compo, 1998) formula (1).

$$127 \quad W(a, b) = \frac{1}{\sqrt{a}} \int_{-\infty}^{\infty} f(t) \psi\left(\frac{t-b}{a}\right) dt \quad (1)$$

128 In the formula,  $\psi(t)$  represents the wavelet basis function, and a and b represent  
 129 the scaling factor and translation parameter of the wavelet function, respectively. In  
 130 order to study the related variability and local periodicity of GIC signals through  
 131 CWT, this paper chooses the Morlet wavelet (Torrence and Compo, 1998) basis  
 132 function as the generating function. Morlet wavelet is a wavelet composed of a  
 133 single-frequency compound exponential function. It is non-orthogonal. Its amplitude  
 134 is modulated by a function proportional to the standard Gaussian function. It has good  
 135 time-frequency localization capabilities. It is often used in the field of space physics  
 136 (Balan et al., 2017). The wavelet expression is shown in formula (2), where  $\xi_0$  is the  
 137 dimensionless frequency.

$$138 \quad \psi(t) = e^{i\xi_0 t} e^{-\frac{t^2}{2}} \quad (2)$$

## 139 2.2. Discrete wavelet transform(DWT)

140 DWT is a wavelet transform that performs discrete sampling of wavelets. In  
 141 DWT analysis, the local regularity in the signal is studied according to the amplitude  
 142 changes of wavelet coefficients (Mendes et al., 2005; Ojeda et al., 2013). The

143 amplitude of the wavelet coefficients may be related to the singularity or discontinuity  
144 of the GIC signal, the calmness or disturbance state of the magnetic field.

145 Since Daubechies wavelet has no symmetry (Daubechies, 1990) it can cause  
146 phase distortion when processing and analyzing signals. Therefore, on this basis, a  
147 Coiflet wavelet (Shyh-Jier and Cheng-Tao, 2002) with a 2N-1 order moment of 0 is  
148 proposed. In this paper, a coif3 wavelet is selected to realize DWT decomposition of  
149 the signal. It decomposes the signal at high and low frequencies, and selects the one  
150 that matches the original signal to decompose again. After three decompositions, three  
151 high-frequency components and one low-frequency component are obtained. Then  
152 analyze the characteristics of the low-frequency and high-frequency components of  
153 the signal and observe the relationship between the decomposed signal and the  
154 original signal. For details, refer Daubechies (1990) and Klausner et al. (2014).

### 155 2.3. Cross wavelet transform

156 Cross wavelet analysis is a new signal analysis technology that analyzes the  
157 correlation of two signals in the time-frequency domain, which is generated by the  
158 combination of cross-spectrum analysis and wavelet transform methods (Grinsted et  
159 al., 2004). It can analyze two time series in time-frequency from multiple time scales.  
160 The correlation between the high-energy region and the low-energy region in the  
161 domain reflects the phase structure and detailed characteristics of the two. It has been  
162 widely used in the fields of meteorology, climate and geophysics. For two time series  
163  $X(t)$  and  $Y(t)$  the cross wavelet power spectrum is as follows (Labat, 2010; Li et  
164 al., 2020):

$$165 \quad W_{XY}(a,b) = W_X(a,b)W_Y^*(a,b) \quad (3)$$

166 where  $W_{XY}(a,b)$  is the cross wavelet power spectrum;  $W_X(a,b)$  is the  
167 sequence  $X(t)$  wavelet transform coefficients, and  $W_Y^*(a,b)$  is the complex of the  
168 sequence  $Y(t)$  wavelet transform coefficients conjugation. Among them,  $a$  is the  
169 scaling parameter and  $b$  is the time translation parameter. The wavelet coherence  
170 spectrum can be used to measure the closeness of the local correlation between two

171 time series in the time-frequency space. The darker the color, the closer the  
 172 correlation between the two. Even if the cross wavelet power spectrum is in the low  
 173 energy region, the two are close in the wavelet coherence spectrum. The degree may  
 174 also be significant. WTC focuses more on the correlation between two time series in  
 175 the low-energy region. The cross wavelet coherence spectrum is defined as follows  
 176 ([Grinsted et al., 2004](#))

$$177 \quad R^2(a,b) = \frac{|S[a^{-1}W_{XY}(a,b)]|^2}{S[a^{-1}W_X(a,b)]S[a^{-1}W_Y(a,b)]} \quad (4)$$

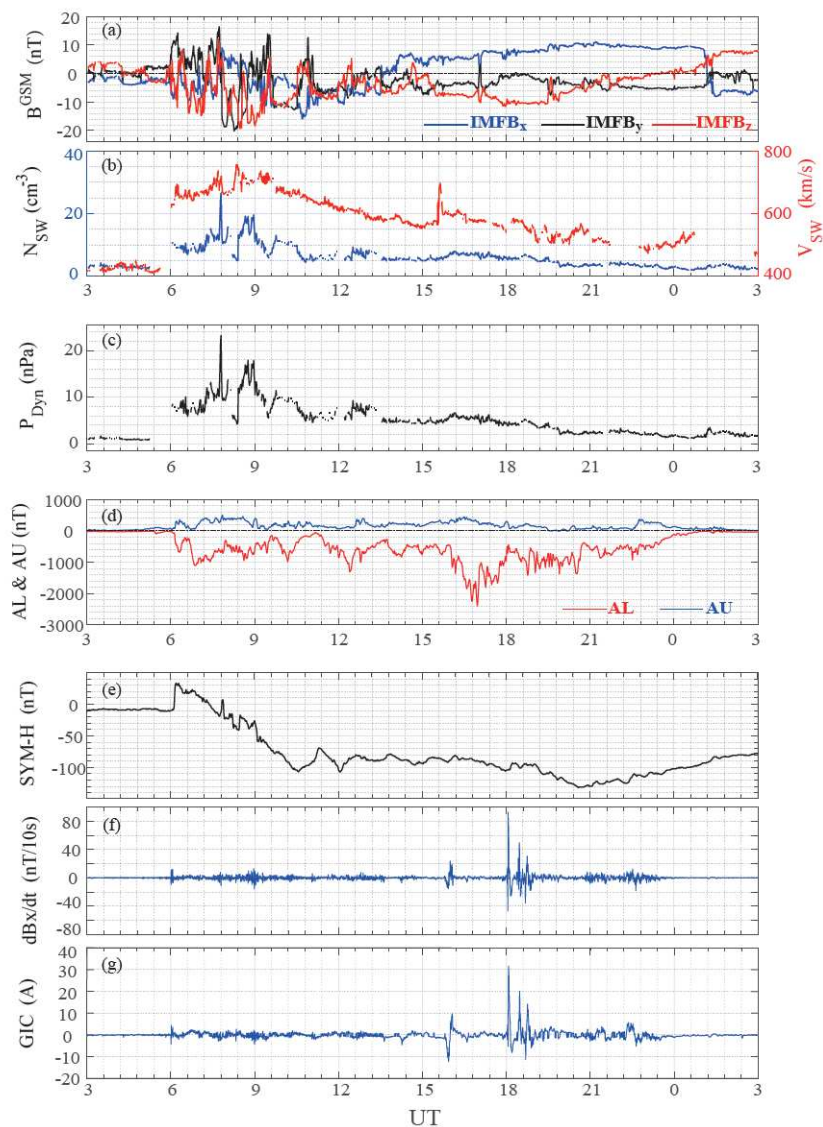
### 178 **3. Results**

#### 179 **3.1. Solar wind, geomagnetic field and GIC**

180 **Figure 1** shows the interplanetary magnetic field (IMF), solar wind parameters,  
 181 geomagnetic indices, and GIC data during the geomagnetic storm on 17 March 2013.  
 182 From top to bottom, the panels show the components of IMF (a), solar wind density  
 183 and speed (b), solar wind dynamic pressure (c), AL and AU indices (d), SYM-H index  
 184 (e), dBx/dt (f), and GIC (g). The resolution of solar wind and interplanetary magnetic  
 185 field parameters is 1 min. In addition, due to the time difference between the bow  
 186 shock and ionosphere, they have a delay of 7 minutes. It can be seen from the figure  
 187 that compared with the calm level before 06 Universal Time (UT), during the period  
 188 from the initial phase, main phase, and recovery phase of the storm until 23:30 UT,  
 189 there are obvious disturbances in all indices.

190 It can be seen from the figure that at 06 UT, there is a sudden change in IMF,  
 191 solar wind parameters, geomagnetic index, dBx/dt index and GIC signal, which is a  
 192 sign of the beginning of geomagnetic emergency. The components of IMF gradually  
 193 stabilized after 15 UT, and Bz was in the southward direction. In AL, it can be seen  
 194 that there are several large substorms, especially around 16UT where a large substorm  
 195 occurred. The SYM-H index reached a minimum value of -132 nT at 20:28 UT,  
 196 indicating that this storm was a major storm. dBx/dt starts to produce disturbances at  
 197 06 UT, the first large disturbance appears at 16 UT, and another larger disturbance  
 198 appear around 18:05 UT, the maximum value reaches 92.9 nT and the disturbance

199 continues until 23:30 UT and gradually returned to a calm level. We speculate that  
 200 this larger disturbance may be related to the influence of the substorm. GIC shows  
 201 small disturbance starting at 06:00 UT, which is similar to the trend of dBx/dt,  
 202 reaching a maximum value of 31.65 A at 18 UT. The disturbance continued until  
 203 23:30 UT and returned to a calm level. It can be seen that GIC and dBx/dt have a high  
 204 similarity in perturbations, so we will study their spectral characteristics in depth.



205

206 **Figure 1.** Overview of solar wind parameters, geomagnetic indices and GIC during 17  
 207 March 2013. From top to bottom: (a) Bx By Bz component of IMF, (b) solar wind velocity  
 208 and solar wind density; (c) solar wind dynamic pressure; (d) AL and AU indices; (e) SYM-H  
 209 index; (f) dBx/dt; (g) GIC.

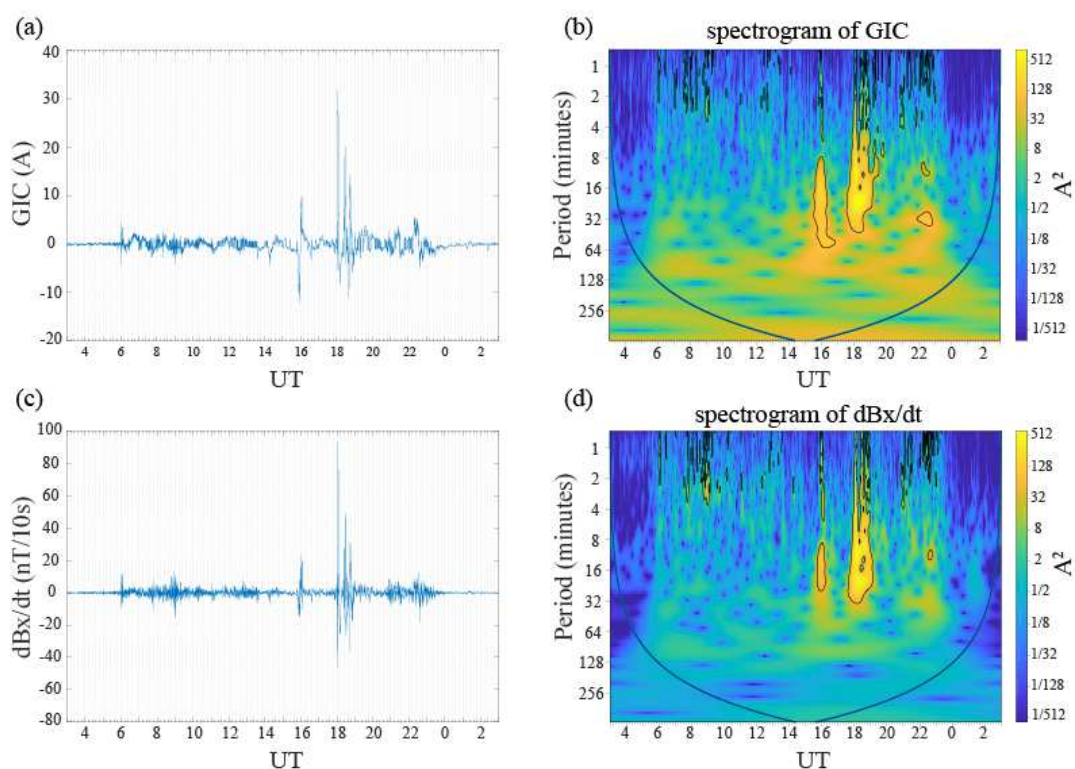
210

### 3.2. Continuous wavelet transform of GIC and dBx/dt

211

**Figure 2a-2b** shows the GIC disturbance and its continuous wavelet transform

212 spectrum. In Figure 2b, the vertical axis is the period, and color blue to yellow  
 213 indicates energy increasing from small to large. The upper part of the thick solid line  
 214 represents the area that passed 95% noise test. It can be seen that in the region from  
 215 06:00UT to 23:30UT, the energy is significantly higher than that of the outer region.  
 216 At the time of first major GIC disturbance at 16 UT, a closed region with period 8-62  
 217 minutes appears in the CWT time-frequency diagram; and around the time of larger  
 218 GIC disturbances at 18-19 UT, a closed area with period 4-48 minutes appears in the  
 219 spectrogram from 17:30UT to 19:30UT. During 22-23 UT, there are two enclosed  
 220 areas with periods of 9-14 min and 29-38 min. There are also some smaller  
 221 oscillations, corresponding to the moments of disturbance in the left figure.



222  
 223 **Figure 2.** (a) Disturbance of GIC; (b) Continuous wavelet spectrogram of GIC; (c)  
 224 Disturbance of dBx/dt; (d) Continuous wavelet spectrogram of dBx/dt.

225

226 **Figure 2c-2d** is similar to Figure 2a-2b but for dBx/dt. In Figure 2c, it can be seen  
 227 that the signal began to disturb from 06:00 UT and lasted until 23:30 UT. The first  
 228 large disturbance appeared at 16 UT, and larger disturbances appeared at 18-19 UT. At  
 229 the same time, the energy increased significantly from 06UT to 23:30UT. A closed  
 230 area with a period of 9-28min appears at 16 UT and another closed area with a period

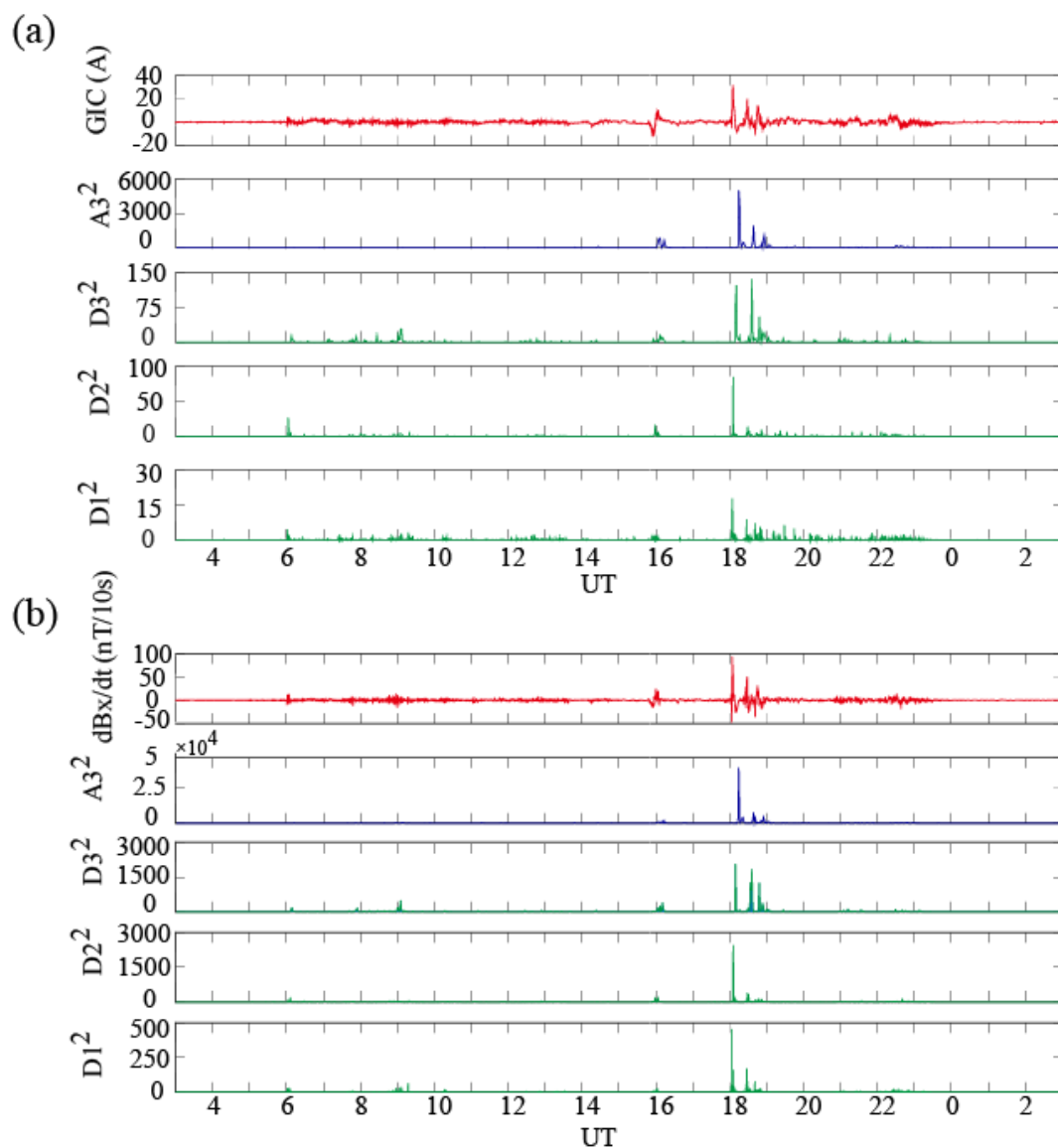
231 of 1-34 min appears from 17UT to 19UT, and a smaller oscillation period appears at  
232 22UT-23UT. There are some smaller oscillation periods in the whole area,  
233 corresponding to the moments when the disturbance is larger in the left picture. As  
234 Figure 2 shows, the frequency spectrum of GIC and dBx/dt have high similarity,  
235 neither has continuous period, and energy in the spectrum corresponds well to the  
236 level of disturbance.

237

### 238 **3.3. Discrete wavelet transform of GIC and dBx/dt**

239

240 **Figure 3** is the discrete wavelet transform diagram of GIC and dBx/dt. From top  
241 to bottom, it shows the square of third-order low-frequency coefficient, third-order  
242 high-frequency coefficient, second-order high-frequency coefficient, and first-order  
243 high-frequency coefficient. The Y-axes scales use large difference for better display.  
244 By comparing the coefficients (**Figure 3a**), it can be seen that the third-order  
245 low-frequency coefficient  $A3^2$  corresponds best to the GIC signal, and the other three  
246 different higher-order signals decrease in amplitude from higher to lower orders. At  
247 around both 16 UT and 18-19 UT, the coefficients have different degrees of  
248 fluctuations, which is consistent with the fluctuation of GIC at the relevant times. It  
249 can be seen from **Figure 3b** that the third-order low frequency corresponds to the best  
250 situation, and the first-order high frequency corresponds to the least ideal situation.  
251 The third-order low frequency signal is the low frequency part obtained by  
252 decomposing the signal three times. After decomposing the third-order low-frequency  
253 part, it still best reflects the characteristics of the original signal. The third-order  
254 low-frequency coefficient reflects the 16 UT and 18-19 UT disturbances of dBx/dt.  
255 The three high-frequency coefficients can be seen to varying degrees in the  
256 disturbances that occur in the entire disturbance interval. As shown, GIC and dBx/dt  
257 have high similarities in wavelet coefficients and high-frequency and low-frequency  
258 characteristics, and both have obvious low-frequency characteristics.



259

260 **Figure 3.** From top to bottom: Discrete Wavelet Transform of GIC (a) and dBx/dt (b). Y-axes  
 261 scales of  $D3^2$ ,  $D2^2$  and  $D1^2$  are expanded compared to that of  $A3^2$  for better display.

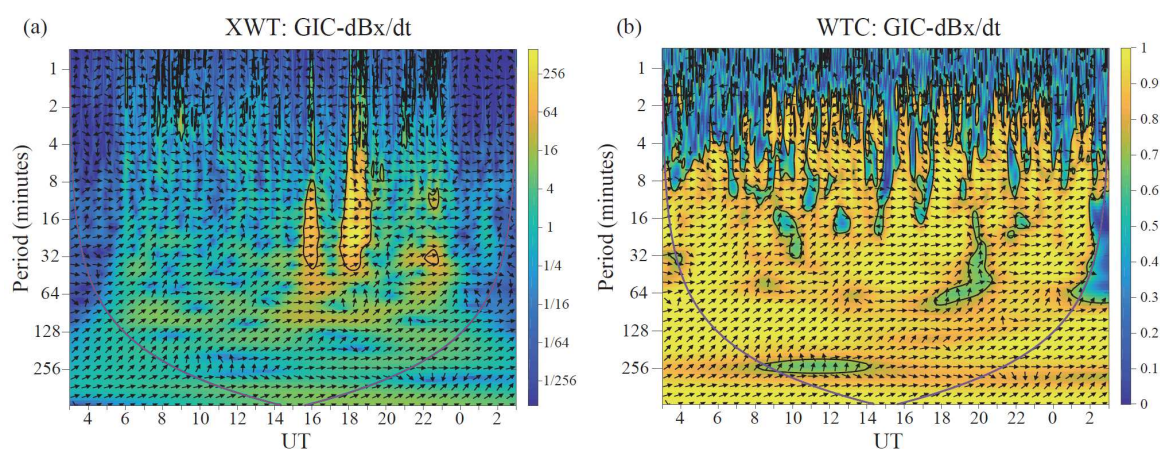
262

### 263 3.4. Cross wavelet transform of GIC and dBx/dt

264

265 **Figure 4a** shows the crossed wavelet power spectrum of GIC and dBx/dt, the vertical  
 266 axis is the period, the color depth represents the size of the crossed GIC and dBx/dt  
 267 power spectrum, and the arrow represents the phase difference between GIC and  
 268 dBx/dt;  $\rightarrow$  indicates that the two are in same phase or positively correlated;  $\leftarrow$   
 269 indicates that the two are in the opposite phase or inversely related;  $\downarrow$  and  $\uparrow$  indicate  
 270 that the latter lags behind and leads the former by  $90^\circ$ . In the figure, the thick solid  
 271 line is the boundary effect cone, and the area above the thick solid line is the area that  
 272 has passed the 95% noise test. It can be seen that in the entire interval from 06:00 UT

273 to 23:30 UT, the energy is significantly higher than the area outside the interval. The  
 274 strongest interaction between GIC and dBx/dt, that is, the cross wavelet high-energy  
 275 area, is mainly concentrated at 15:30-16:30 UT and 17:30-19:10 UT. There are two  
 276 obvious enclosed areas with a period of 8-42 minutes and 2-42 minutes. There are two  
 277 small areas in 22-23 UT, the period is 10-14 min and 28-38 min respectively. In the  
 278 four obvious areas, the arrow points to the upper right as a whole, indicating that  
 279 dBx/dt precedes over GIC, there is a positive correlation between the two to a certain  
 280 extent, and there are some small periodic oscillation signals with a small area.



281

282 **Figure 4.** (a) Cross wavelet transform of GIC and dBx/dt, and (b) Wavelet transform coherence  
 283 of the GIC and dBx/dt.

284

285 **Figure 4b** shows the cross-wavelet coherence spectrum of GIC and dBx/dt, where  
 286 the color depth represents the correlation between the two, yellow represents strong  
 287 correlation and blue poor correlation; and the remaining parameters are the same as  
 288 for Figure 4a. It can be seen that the area enclosed by the black line occupies most of  
 289 the entire time series, and the correlation coefficient of some areas is close to 1, and  
 290 the arrow in the area points to the upper right as a whole, indicating that the  
 291 correlation between GIC and dBx/dt is not limited to the duration of the magnetic  
 292 storm. On quiet days also the correlation between the two is strong, and dBx/dt occurs  
 293 before GIC.

#### 294 4. Discussion and conclusions

295 As mentioned in the introduction, GIC is a non-stationary periodic signal that is

---

296 continuously transformed in time. Therefore, many scientists have used CWT  
297 (continuous wavelet transform) to conduct excellent research on the GIC spectrum  
298 (Xu, 2011; Khanal et al., 2019). These studies found that GIC has short-term energy  
299 bursts and there is no continuous periodicity. Falayi et al. (2017) used CWT to  
300 perform spectrum analysis on GIC and found that GIC corresponds well to the  
301 high-energy wavelet coefficients of dBx/dt. With a view to establish a forecasting tool  
302 for geomagnetic disturbances, Adhikari et al. (2017) used CWT and DWT (discrete  
303 wavelet transform) to analyze the GIC data during geomagnetic storms, and found  
304 that GIC has stronger power spectrum in response to magnetic storms. However,  
305 earlier studies have not used CWT and DWT together to study GIC and geomagnetic  
306 data, and no study has analyzed the correlation between GIC and geomagnetic data  
307 using cross wavelet transform (XWT) or wavelet coherence (WTC) techniques. In this  
308 paper, considering the data during the intense geomagnetic storm on 17 March 2013,  
309 we have shown the feasibility of using CWT and DWT together to analyze the  
310 spectrum and wavelet coefficients of both GIC and dBx/dt. Then, XWT and WTC  
311 techniques are used to analyze the correlation and phase relationship between GIC  
312 and dBx/dt in time and frequency domain for the first time.

313

314 The GIC and dBx/dt data have two occasions of larger disturbance at ~16 UT  
315 and 18 UT when IMF Bz remained southward. At ~16 UT, the AL index decreases  
316 rapidly, resulting in a larger geomagnetic substorm. At 18UT, both GIC and dBx/dt  
317 have larger disturbances, AL index has just recovered from minimum value, and more  
318 frequency changes appeared. The changes of GIC and dBx/dt can be distinguished by  
319 solar wind parameters and SYM-H index. However, the extreme values of GIC are  
320 related more to IMF Bz southward and geomagnetic substorms (Falayi and Beloff,  
321 2012). GIC has high correlation with dBx/dt fluctuation, which is consistent with the  
322 results of Viljanen (1997).

323

324 The CWT spectra of GIC and dBx/dt show large similarities, there is no  
325 continuous periodicity, and two high-energy enclosed areas with good correspondence

---

326 exist; this indicates a certain correlation between GIC and  $dBx/dt$ . This is similar to  
327 the conclusions of an earlier study (Khanal et al., 2019). Through DWT analysis of  
328 GIC and  $dBx/dt$ , it is found that the wavelet coefficient increases significantly when  
329 the GIC disturbance is large. And the third-order low-frequency coefficient best  
330 reflects the disturbance of GIC and illustrates the low-frequency characteristics of  
331 GIC, which has quasi-DC characteristics. The third-order low frequency coefficient is  
332 the low frequency part of the original signal obtained by decomposing the high and  
333 low frequencies three times. The wavelet coefficient of  $dBx/dt$  is similar to GIC,  
334 indicating that the two have high similarity and there is a certain correlation. This is  
335 similar to the conclusion obtained by (Adhikari et al., 2019) on the discrete wavelet  
336 analysis of geomagnetic components.

337

338 The cross wavelet (XWT) and wavelet coherence (WTC) method can be used as  
339 a new method to analyze the temporal and spatial changes of GIC and  $dBx/dt$  or other  
340 geomagnetic indices. The cross-wavelet aggregation spectrum and the cross-wavelet  
341 coherence spectrum clearly show the correlation, phase difference and local  
342 characteristics between the two signals in the time-frequency domain. It also passed  
343 the 95% confidence test, indicating high reliability. Thus, we use the XWT and WTC  
344 to investigate correlation and phase relationship of GIC and  $dBx/dt$  in time-frequency  
345 domain in this paper for the first time. Through XWT and WTC analysis, we found  
346 that GIC and  $dBx/dt$  have a very strong correlation; and at times of large disturbance,  
347 the arrow direction points to the upper right, indicating that  $dBx/dt$  is ahead of GIC  
348 and there is a positive correlation between GIC and  $dBx/dt$  to a certain extent. From  
349 the WTC, it can be seen that the yellow enclosed area occupies most of the space,  
350 indicating that the correlation between  $dBx/dt$  and GIC is relatively strong both during  
351 magnetic storms and non-magnetic storms, and  $dBx/dt$  occurs before GIC. Changes in  
352 GIC play a leading role, and  $dBx/dt$  is the main cause of GIC. This also proves that  
353 the cross wavelet method is also suitable for studying the relationship between GIC  
354 and geomagnetic index. In the future, we can use cross wavelet to analyze the phase  
355 characteristics and correlation between interplanetary parameters and GIC.

356

---

## 357 **Abbreviations**

358 GIC: Geomagnetically Induced Current; CWT: Continuous Wavelet Transform; DWT:  
359 Discrete Wavelet Transform; XWT: Cross Wavelet Transform; WTC: Wavelet  
360 Coherence; IMF: Interplanetary Magnetic Field; UT: Universal Time.

361

## 362 **Acknowledgements**

363 We thank the Finnish Meteorological Institute and Gasum Company for recording and  
364 providing GIC data. We thank the INTERMAGNET for providing geomagnetic field  
365 data. We also thank OMNIWEB for providing solar wind, IMF and geomagnetic data.

366

## 367 **Authors' contributions**

368 ZX and LL conceived the idea and performed research; WX, NB and ZX wrote the  
369 manuscript; YW, QZ , WL and ZS analyzed data and participated in the scientific  
370 discussions. All authors read and approved the final manuscript.

371

## 372 **Funding**

373 This study is supported by the National Natural Science Foundation (Grants  
374 41904169, 41604139, 41874170 and 41831072), and the foundation of National Key  
375 Laboratory of Electromagnetic Environment (6142403180103, 6142403180102).

376

## 377 **Availability of data and materials**

378 The GIC data can be found from this webpage [http://space.fmi.fi/gic/man\\_ascii](http://space.fmi.fi/gic/man_ascii). The  
379 geomagnetic field data are came from INTERMAGNET  
380 (<https://space.fmi.fi/image/www/index.php>). The solar wind, IMF and geomagnetic  
381 index data are available from the OMNIWEB (<https://omniweb.gsfc.nasa.gov/>).

382

## 383 **Competing interests**

384 The authors declare no competing interests.

385

## 386 References

- 387 Adhikari B, Khatiwada R, Chapagain N P. 2017. Analysis of Geomagnetic Storms Using Wavelet  
388 Transforms. *Journal of Nepal Physical Society*, 4(1), 119-124
- 389 Adhikari B, Sapkota N, Dahal S, Bhattarai B, Khanal K, Chapagain N. 2019. Spectral  
390 characteristic of geomagnetically induced current during geomagnetic storms by wavelet  
391 techniques. *Journal of Atmospheric and Solar-Terrestrial Physics*, 192: 104777.
- 392 Albertson VD, Thorson, JM. 1974. Power system disturbances during a K-8 geomagnetic storm:  
393 August 4, 1972. *IEEE Transactions on Power Apparatus and Systems*, PAS-93(4):  
394 1025-1030.
- 395 Ariannik M, Rezaei-Zare A, Werle P. 2020. Processing Magnetometer Signals for Accurate  
396 Wide-Area Geomagnetic Disturbance Monitoring and Resilience Analysis. *IEEE*  
397 *Transactions on Power Delivery*: p. 1-1.
- 398 Balan N, Ebihara Y, Skoug R, Shiokawa K, Batista IS, Tulasi Ram S, Omura Y, Nakamura T, Fok  
399 M-C. 2017. A scheme for forecasting severe space weather. *Journal of Geophysical Research:*  
400 *Space Physics*, 122(3): 2824-2835.
- 401 Bolduc, L. 2002. GIC observations and studies in the Hydro-Quebec power system. *mos. Sol. Terr.*  
402 *Phys.* 64 (16), 1793–1802.
- 403 Boteler, DH, Jansen van Beek G. 1999. August 4, 1972 revisited: A new look at the geomagnetic  
404 disturbance that caused the L4 cable system outage. *Geophysical research letters*. 26(5): p.  
405 577-580.
- 406 Campbell WH. 1978. Induction of auroral zone electric currents within the Alaskan pipeline. *Pure*  
407 *Appl. Geophys.* 116, 1143–1173. <https://doi.org/10.1007/BF00874677>.
- 408 Carrington RC. 1859. Description of a singular appearance seen in the Sun on September 1,  
409 1859, *Mon. Not. R. Astron. Soc.*, XX, 13.
- 410 Daubechies I. 1990. The wavelet transforms time-frequency localization and signal analysis. *IEEE*  
411 *Trans. Inf. Theor.* 36 (5), 961–1005.
- 412 Dimmock AP, Rosenqvist L, Hall J-O, Viljanen A, Yordanova E, Honkonen I, André M, Sjöberg E  
413 C. 2019. The GIC and Geomagnetic Response Over Fennoscandia to the 7–8 September  
414 2017. *Geomagnetic Storm*, 17(7) 989-1010, doi: 10.1029/2018SW002132
- 415 Eroshenko EA, Belov AV, Boteler D, Gaidash SP, Lobkov SL, Pirjola R, Trichtchenko L. 2010.  
416 Effects of strong geomagnetic storms on Northern railways in Russia. *Advances in Space*  
417 *Research.* 46(9): p. 1102-1110.
- 418 Falayi EO, Beloff N. 2012. Modelling of geomagnetically induced currents during geomagnetic  
419 storms using geoelectric fields and auroral electrojet indices. *Indian J. Phys.* 86 (6), 423–429.  
420 <http://dx.doi.org/10.1007/s12648-012-0108-0>.
- 421 Falayi EO, Ogunmodimu O, Bolaji OS, Ayanda JD, Ojoniyi OS. 2017. Investigation of  
422 geomagnetic induced current at high latitude during the storm-time variation. *NRIAG Journal*  
423 *of Astronomy and Geophysics*, 6(1): 131-140.
- 424 Gideon DN, Hopper AT, Thompson RE. 1970. Earth Current Effects on Buried Pipelines: Analysis  
425 of Observations of Telluric Gradients and Their Effects. *American Gas Assn., Cat. No. L*

- 426 30570, 77 pp.
- 427 Grinsted A, Moore JC, Jevrejeva S. 2004. Application of the Cross Wavelet Transform and  
428 Wavelet Coherence to Geo-physical Time Series. *Nonlinear Processes in Geophysics*,  
429 11(5-6):561-566.
- 430 Heyns MJ, Gaunt CT, Lotz SI, Ciliers PJ. 2020. Data driven transfer functions and transmission  
431 network parameters for GIC modelling. *Electric Power Systems Research*, 188: p. 106546.
- 432 Juusola L, Vanhamaki H, Viljanen A, Smirnov M. 2020. Induced currents due to 3D ground  
433 conductivity play a major role in the interpretation of geomagnetic variations. *Annales*  
434 *Geophysicae*, 38(5): p. 983-998.
- 435 Khanal K, Adhikari B, Chapagain NP, Bhattarai B. 2019. HILDCAA-related GIC and possible  
436 corrosion hazard in underground pipelines: a comparison based on wavelet transform. *Space*  
437 *Weather*, 17(2): 238-251.
- 438 Klausner V, Mendes O, Domingues MO, Papa ARR, Tyler RH, Frick P, Kherani EA. 2014.  
439 Advantage of wavelet technique to highlight the observed geomagnetic perturbations linked  
440 to the chilean tsunami. *Geophys. Res. 119*,3077–3093.
- 441 Labat, D. 2010. Cross wavelet analyses of annual continental freshwater discharge and selected  
442 climate indices. *Journal of Hydrology*. 385(1-4): p. 269-278.
- 443 Li YL, Wen YL, Lai HX, Zhao QQ. 2020. Drought response analysis based on cross wavelet  
444 transform and mutual entropy. *Alexandria Engineering Journal*, 59(3): 1223-1231.
- 445 Liu C, Liu LG, Pirjola R. 2009. Geomagnetically Induced Currents in the High-Voltage Power  
446 Grid in China. *IEEE Transactions on Power Delivery*, 24(4): p. 2368-2374.
- 447 Mendes OJ, Domingues MO, Costa AM. 2005. Wavelet analysis applied to magneto-grams. *Atmos.*  
448 *Sol. Terr. Phys.* 67, 1827–1836.
- 449 Ngwira C, and Pulkkinen A. 2019. An Introduction to Geomagnetically Induced Currents.  
450 *Geomagnetically Induced Currents from the Sun to the Power Grid. Geophysical Monograph*  
451 244, First Edition p.3-14.
- 452 Ojeda GA, Mendes OJ, Calzadilla MA, Domingues MO. 2013. Spatio-temporal entropy analysis  
453 of the magnetic field to help magnetic cloud characterization. *Geophys. Res. Space Phys.* 118,  
454 5403–5414. <https://doi.org/10.1002/jgra.50504>.
- 455 Pirjola R. 2000. Geomagnetically induced currents during magnetic storms. *IEEE Transactions on*  
456 *Plasma Science*, 28(6), 1867-1873.
- 457 Pulkkinen A, Kataoka R. 2006. S-transform view of geomagnetically induced currents during  
458 geomagnetic superstorms. *Geophysical Research Letters*, 33(12).
- 459 Pulkkinen A, Viljanen A, Pajunpa K, Pirjola R. 2001. Recordings and occurrence of  
460 geomagnetically induced currents in the Finnish natural gas pipeline network. *Appl. Geophys.*  
461 48, 219231
- 462 Shyh-Jier H, Cheng-Tao H. 2002. Coiflet wavelet transform applied to inspect power system  
463 disturbance-generated signals. *IEEE Transactions on Aerospace and Electronic Systems*, vol.  
464 38, no. 1, pp. 204-210. doi: 10.1109/7.993240.
- 465 Torrence C, Compo GP. 1998. A Practical Guide to Wavelet Analysis, *Bull. Am. Meteor. Soc.*, 79,  
466 61–78.
- 467 Tóth G, Meng X, Gombosi TI, Rastätter L. 2014. Predicting the time derivative of local magnetic  
468 perturbations. *Journal of Geophysical Research: Space Physics*, 119(1): p. 310-321.
- 469 Trichtchenko L, Boteler DH. 2004. Modeling geomagnetically induced currents using  
470 geomagnetic indices and data. *IEEE Transactions on Plasma Science*, 32(4): p. 1459-1467.

- 
- 471 Viljanen A, Nevanlinna H, Pajunpää K, Pulkkinen A. 2001. Time derivative of the horizontal  
472 geomagnetic field as an activity indicator. *ANNALES GEOPHYSICAE*. 19(9): p. 1107-1118.  
473 Viljanen A. 1997. The relation between geomagnetic variations and their time derivatives and  
474 implications for estimation of induction risks. *Geophys. Res. Lett.* 24  
475 doi:10.1029/97GL00538.  
476 Xu ZH. 2011. Study of Geomagnetic Disturbances and Ring Current Variability during Storm and  
477 Quiet Times Using Wavelet Analysis and Ground-based Magnetic Data from Multiple  
478 Stations. *All Graduate Theses and Dissertations*, p. 984.  
479

## 480 **Figure captions**

481 **Fig. 1.** Overview of solar wind parameters, geomagnetic indices and GIC during 17 March  
482 2013. From top to bottom: (a) Bx By Bz component of IMF, (b) solar wind velocity and solar  
483 wind density; (c) solar wind dynamic pressure; (d) AL and AU indices; (e) SYM-H index; (f)  
484 dBx/dt; (g) GIC.

485

486 **Fig. 2.** (a) Disturbance of GIC; (b) Continuous wavelet spectrogram of GIC; (c) Disturbance  
487 of dBx/dt; (d) Continuous wavelet spectrogram of dBx/dt.

488

489 **Fig.3.** From top to bottom: Discrete Wavelet Transform of GIC (a) and dBx/dt (b). Y-axes scales  
490 of  $D3^2$ ,  $D2^2$  and  $D1^2$  are expanded compared to that of  $A3^2$  for better display.

491

492 **Fig. 4.** (a) Cross wavelet transform of GIC and dBx/dt, and (b) Wavelet transform coherence of  
493 the GIC and dBx/dt.

# Figures

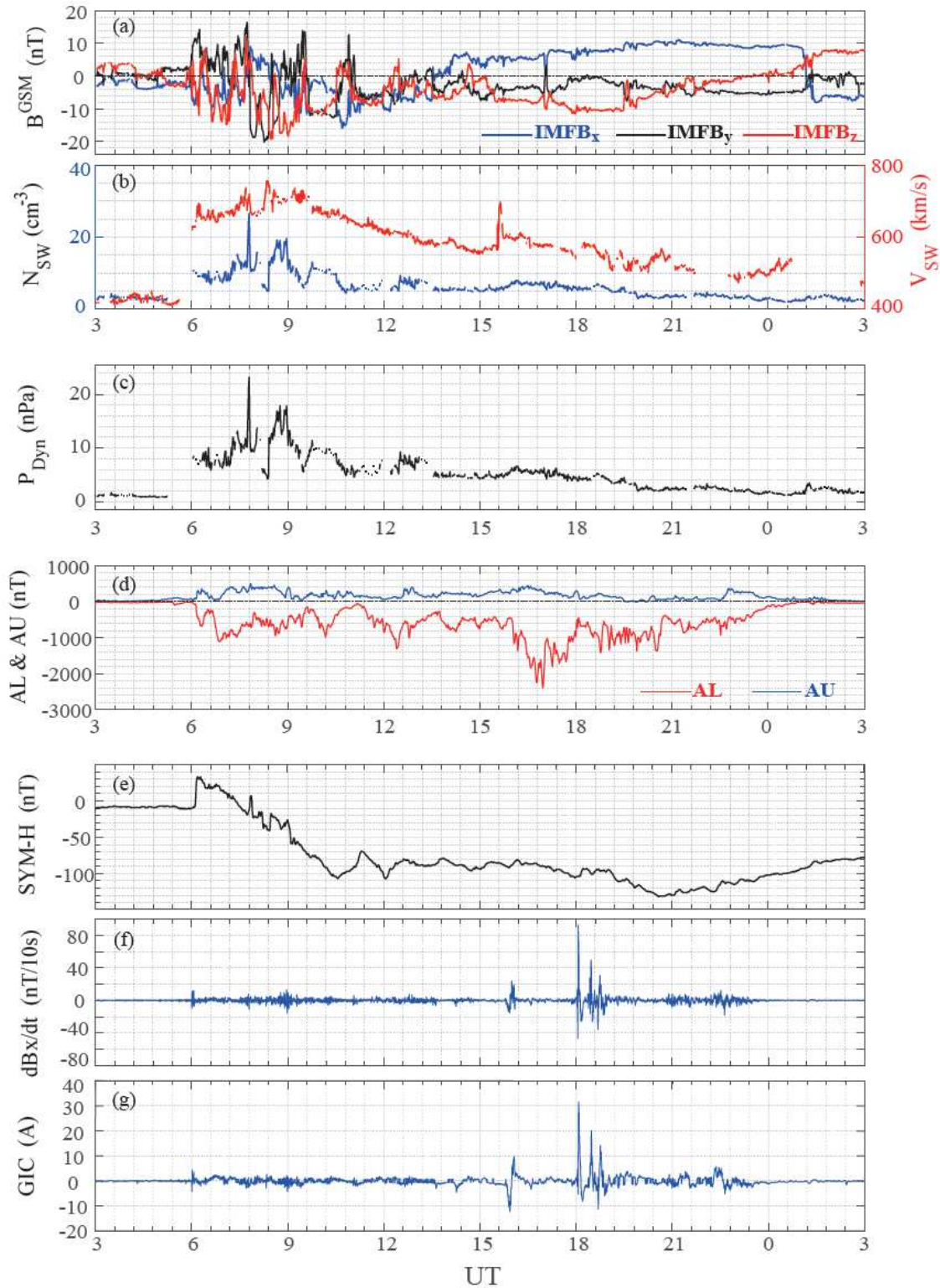


**Figure 1**

Overview of solar wind parameters, geomagnetic indices and GIC during 17 March 2013. From top to bottom: (a) Bx By Bz component of IMF, (b) solar wind velocity and solar wind density; (c) solar wind dynamic pressure; (d) AL and AU indices; (e) SYM-H index; (f) dBx/dt; (g) GIC.

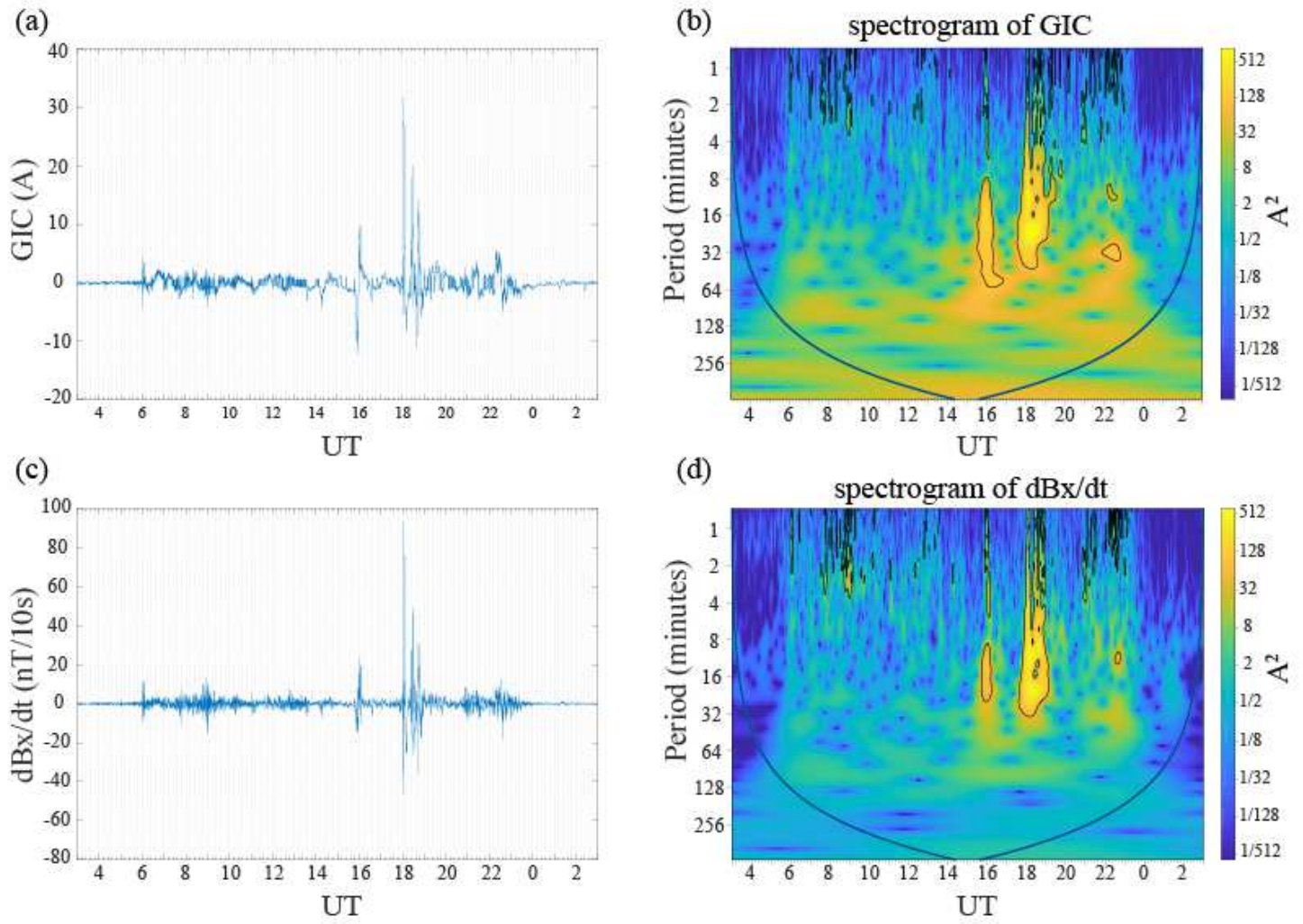


**Figure 2**

(a) Disturbance of GIC; (b) Continuous wavelet spectrogram of GIC; (c) Disturbance of dBx/dt; (d) Continuous wavelet spectrogram of dBx/dt.

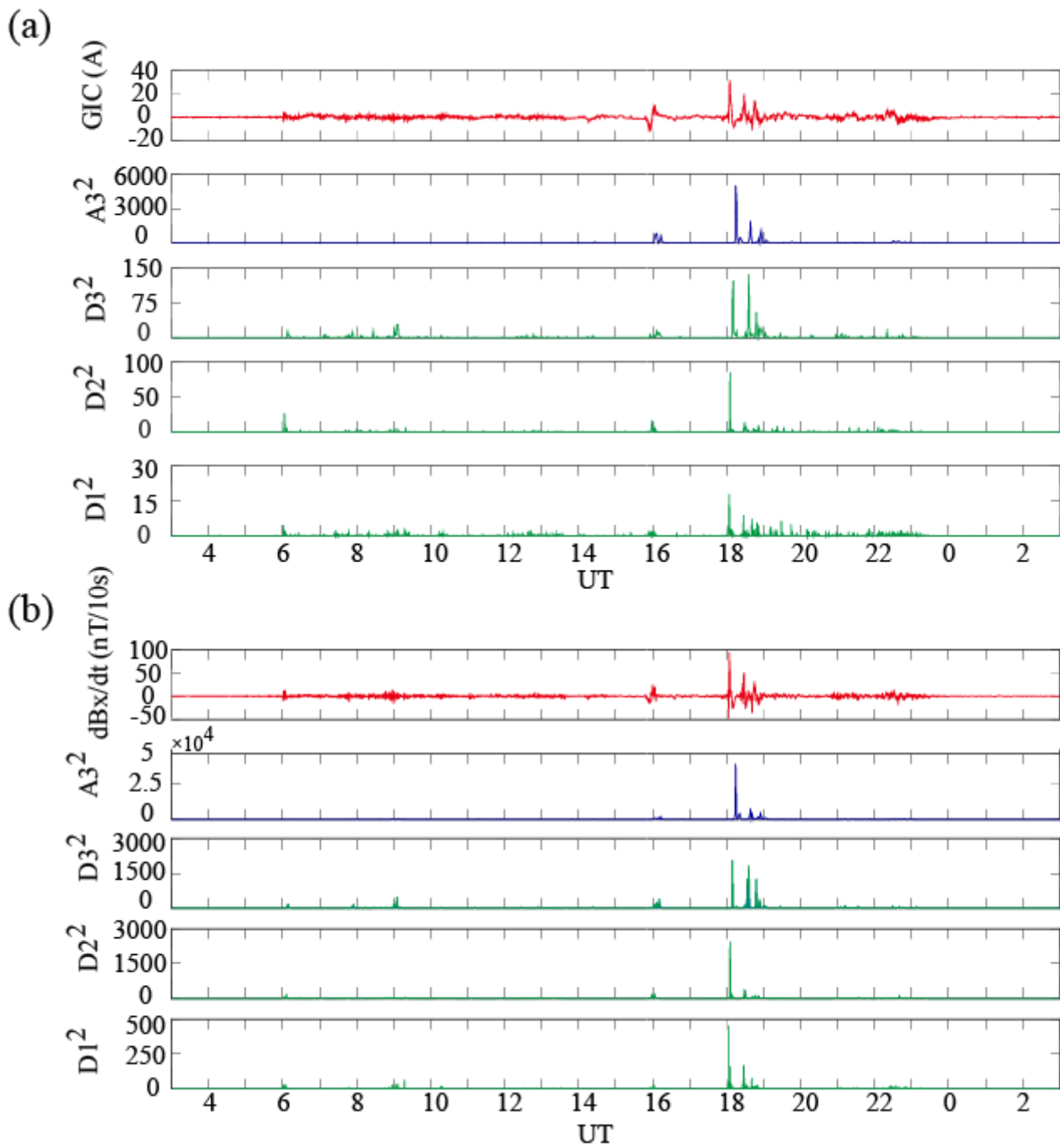


**Figure 3**

From top to bottom: Discrete Wavelet Transform of GIC (a) and dBx/dt (b). Y-axes scales of D32, D22 and D12 are expanded compared to that of A32 for better display.

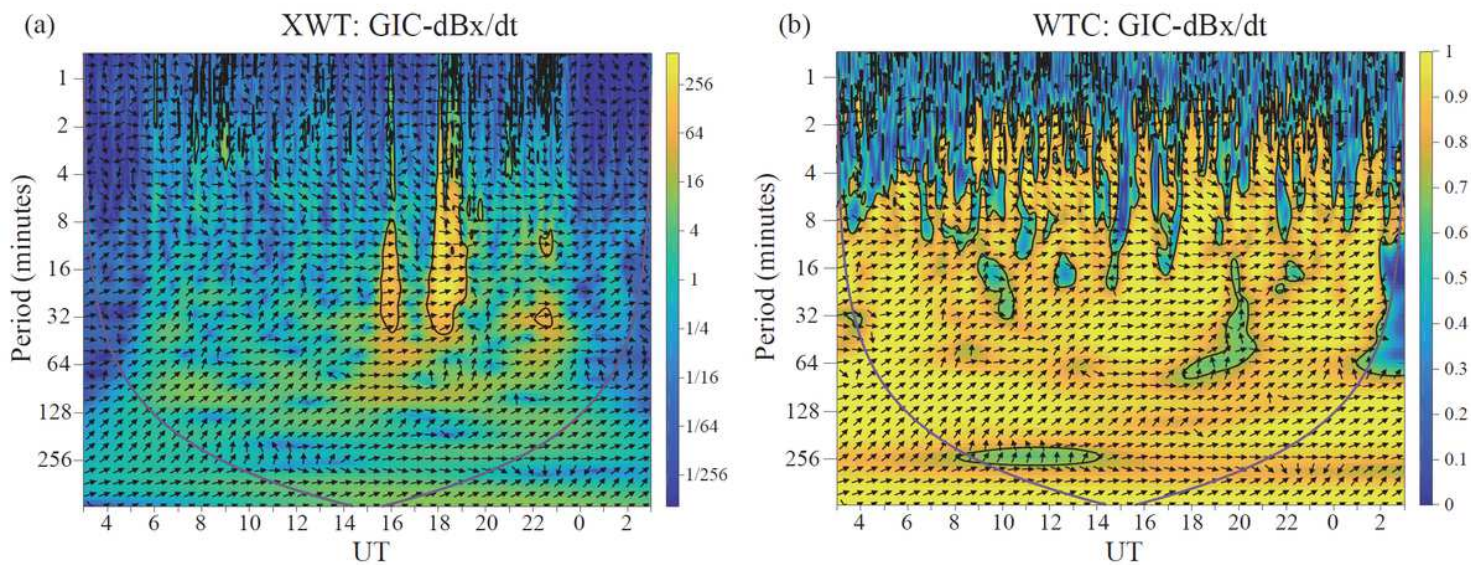


**Figure 4**

(a) Cross wavelet transform of GIC and dBx/dt, and (b) Wavelet transform coherence of the GIC and dBx/dt.

## Supplementary Files

This is a list of supplementary files associated with this preprint. Click to download.

- [GraphicalAbstract.jpg](#)